Electronic Supplementary Material (ESI) for Chemical Communications.

Electronic Supplementary Information for

Piezoelectricity-enhanced photoelectrochemistry synthesis of H_2O_2 on an Au nanoparticles modified p-type Sb-doped ZnO nanotubes array

Jun Cheng, Chenpu Chen, Mingjian Chen, Qingji Xie*

Key Laboratory of Chemical Biology & Traditional Chinese Medicine Research (Ministry of Education of China), College of Chemistry and Chemical Engineering, Hunan Normal University, Changsha 410081, China

---

[*] Corresponding author.
E-mail address: xieqj@hunnu.edu.cn (Q.J. Xie)

Experimental Section

Materials and instrumentation

Acetone, ethanol, zinc acetate, monoethanolamine (MEA), 2-methoxyethanol, zinc nitrate, hexamethylenetetramine (HMT), glycolic acid, sodium hydroxide, antimony acetate, chloroauric acid, methanol, sodium sulfate, hydrogen peroxide, titanium tetrachloride, hydrochloric acid, dimethyl sulfoxide (DMSO), tetrabutylammonium hexafluorophosphate (Bu_4NPF_6) and benzoyl chloride (BzCl) were purchased from Sinopharm Chemical Reagent Co., Ltd. (Shanghai, China). All reagents were of analytical grade or higher purity and not further purified before use. The indium tin oxide (ITO) slices (type P003, sheet resistance < 15 Ω cm^{-2}, and the effective area of each modified ITO electrode was limited to 1 cm^2 using an insulating tape.) were purchased from Ningbo Kaiwo photoelectric Technology Co., Ltd. (Ningbo, China). Milli-Q ultrapure water (Millipore, ≥ 18 MΩ cm) was used throughout.

All electrochemical experiments, such as cyclic voltammetry (CV), linear sweep voltammetry (LSV), current-time (*i*-*t*) and electrochemical impedance spectroscopy (EIS) experiments were performed on a CHI660E electrochemical workstation (CH Instruments Inc., USA). The EIS was analyzed by the Z-View software (Scribner Associates Inc., USA). A 100 mW cm^{-2} Hg lamp (from a 500 W Hg lamp, CEL-M500, Ceaulight, China) was employed in the ultrasound-assisted photodeposition (PD) experiments. All photoelectrochemistry (PEC) experiments, such as LSV under chopped-light illumination, transient photocurrent density responses at 0.4 V constant potential, open circuit potential (V_{OC})-time (V_{OC}-t), incident photon-electron conversion efficiency (IPCE) and Mott-Schottky experiments were performed on a ZAHNER electrochemical workstation equipped with a

CIMPS-IPCE (ZAHNER, Germany). The light power density of monochromatic light was measured by a series of optical filters (5 nm bandwidth, from 365 to 800 nm) and a CEL-FZ-A optical power density meter (Ceaulight, China). The conventional three-electrode system was adopted, with bare or modified ITO photoelectrode as the working electrode (WE), a Pt mesh as the counter electrode (CE), and an Ag/AgCl/KCl(sat.) electrode as the reference electrode (RE). The potentials vs Ag/AgCl/KCl(sat.) are revised to those vs reversible hydrogen electrode (RHE) according to $E_{\mathrm{RHE}} = E_{\mathrm{Ag/AgCl/KCl(sat.)}} + 0.05916\mathrm{pH} + 0.198$ (25 $^{\circ}$C).[1] Scanning electron microscopy (SEM) images and energy dispersive spectroscopy (EDS) results were obtained on a SEM450 field emission scanning electron microscope (FEI, Czech) with EDS function. X-ray diffraction (XRD) patterns were recorded on an Ultima IV X-ray diffractometer (Rigaku, Japan) and analyzed by JCPDS standard cards. X-ray photoelectron spectroscopy (XPS) patterns were recorded on an Escalab-250xi X-ray photoelectron spectrometer (Thermo Fisher Scientific, USA). Piezoresponse force microscopy (PFM) test was performed on an atomic force microscope (AFM, Shimadzu SPM9700). Ultraviolet-visible (UV-vis) diffuse reflectance spectroscopy (DRS, 350 ~ 750 nm) was recorded on an U-3310 UV-vis spectrophotometer (Hitachi, Japan) with $BaSO_4$ as the reference. UV-vis photoluminescence (PL) spectroscopy (325 ~ 650 nm, excited at 325 nm) was recorded on a F-4500 fluorescence spectrophotometer (Hitachi, Japan).

Preparation of modified electrodes

The $\mathrm{Au_{NP}/p\text{-}ZnO_{Sb,NT}/ITO}$ photoelectrode with photoelectric and piezoelectric dual activity was prepared by the four steps shown in Scheme 1A. (1) The ITO slice was ultrasonically treated in water, acetone, ethanol and water each for 10 min to remove surface impurities.

Zinc acetate was dissolved in 2-methoxyethanol, MEA as a stabilizer was then added (both 50 mM final concentrations), and the mixture was stirred at 60 °C for 2 h and aged at room temperature for 24 h. The mixed solution was then uniformly coated on the conductive surface of ITO by a spin coater (3000 rpm), and the coated ITO slice was annealed at 350 °C for 30 min to evaporate the solvent and remove unreacted species. The above operation was repeated three times to obtain a dense ZnO seed (ZnO_{seed}) layer modified ITO substrate (ZnO_{seed}/ITO). (2) The ZnO_{seed}/ITO substrate was placed in an autoclave containing 50 mM $Zn(NO_3)_2$ + 50 mM HMT + 1 mM $Sb(Ac)_3$ + 12 mM sodium glycolate ($C_2H_3O_3Na$) aqueous solution for 24 h reaction at 95 °C to obtain a p-$ZnO_{Sb,NR}$/ITO electrode. Here, the ZnO_{seed}/ITO slice was placed at a 45° angle against the Teflon inner wall of the autoclave, with the conductive ITO surface facing down, in order to ensure the slow growth of ZnO_{NR} on the ZnO_{seed}/ITO surface and avoid the gravity-induced sedimentation of ZnO. In addition, $Sb(Ac)_3$ was first dissolved in aqueous sodium glycolate to minimize its hydrolyzation by forming their soluble coordination compounds. (3) The p-$ZnO_{Sb,NT}$/ITO electrode was prepared by immersing the p-$ZnO_{Sb,NR}$/ITO electrode in 0.15 M aqueous NaOH at 85 °C for 40 min. (4) The Au_{NP}/p-$ZnO_{Sb,NT}$/ITO electrode was prepared by simultaneous Hg-lamp irradiation and ultrasonic treatment of the p-$ZnO_{Sb,NT}$/ITO electrode for 5 min in 0.25 mM aqueous $HAuCl_4$ containing 5% (volume percentage) CH_3OH, and a red-colored Au_{NP}-containing solution was also obtained.

An Au_{NP}/ITO electrode was prepared by dropping 100 μL of the above Au_{NP}-containing solution on an ITO surface and drying in an oven at 60 °C.

An n-type TiO_2 nanorods (n-$TiO_{2,NR}$) array modified ITO (n-$TiO_{2,NR}$/ITO) electrode was prepared by placing a bare ITO substrate in an autoclave containing 4 M HCl + 0.15 M $TiCl_4$ aqueous solution for 18 h reaction at 150 ^{o}C.[2]

Electrochemistry measurements and PPEC-ORR

EIS experiments of various electrodes in 0.5 M aqueous Na_2SO_4 containing 2 mM $K_4[Fe(CN)_6]$ were conducted to evaluate the electron transfer resistance (R_{et}), with experimental parameters given later. The effect of piezoelectric effect on the PEC performance was evaluated by changing the solution-stirring rate (0 ~ 1500 rpm). LSV experiments (1 ~ 0 V, 10 mV s^{-1}) were employed to evaluate the potential dependence of photocurrent density (j, mA cm^{-2}). V_{OC}-t experiments were employed to evaluate the lifetime (τ) of photoelectrons on the conduction band (CB). Mott-Schottky experiments (-0.6 ~ 1.2 V, 10 mV s^{-1}) were employed to evaluate the semiconductor types and calculate the carrier density (N). IPCE experiments were employed to evaluate the incident photon-electron conversion efficiencies of semiconductors at different wavelength.

The PPEC-ORR was performed in a quartz two-chamber PEC cell, with the cathode compartment (working and reference electrodes) and the anode compartment (counter electrode) connected by a Nafion membrane to inhibit the electrochemical oxidation of H_2O_2 to O_2 at the anode. The prepared Au_{NP}/p-$ZnO_{Sb,NT}$/ITO, p-$ZnO_{Sb,NT}$/ITO or p-$ZnO_{Sb,NR}$/ITO electrode was employed as the working electrode, Ag/AgCl/KCl(sat.) as the reference electrode, and the Pt mesh as the counter electrode. The electrolyte in the cathodic chamber was O_2-saturated 0.5 M aqueous Na_2SO_4 at 10 ^{o}C (ice bath, to prevent the thermal decomposition of H_2O_2), the electrolyte in the anodic chamber was 0.5 M aqueous Na_2SO_4, and the light source was 100 mW cm^{-2} AM 1.5G simulated sunlight. The chemical reactions are $O_2 + 2H^+ + 2e^- = H_2O_2$ (photocathode) and $2H_2O = O_2 + 4H^+ + 4e^-$ (Pt anode). In the PPEC-ORR process, O_2 bubbles were continuously blown into the cathode chamber, and the p-$ZnO_{Sb,NT}$ of Au_{NP}/p-$ZnO_{Sb,NT}$/ITO electrodes could be bent to generate the piezoelectric electric field with continuous solution stirring. The produced H_2O_2 was sampled every 10 min and immediately placed in the refrigerator to prevent H_2O_2 from being decomposed by heat.

Analysis of H_2O_2

The yield of H_2O_2 was determined by UV-vis spectrophotometry.[3] Standard 0 mM, 0.4 mM, 0.8 mM, 1.2 mM, 1.6 mM and 2.0 mM aqueous H_2O_2 were prepared from 30% H_2O_2. Take 50 μL of each standard solution or PPEC-ORR sample solution, add 450 μL of 1 M aqueous HCl containing 10 mM $FeSO_4$, and let stand for 30 min after mixing, measure the absorbance of Fe^{3+} at 330 nm, and calculate Fe^{3+} concentration by the Lambert-Beer law. The concentration of H_2O_2 is converted by the reaction formula $2Fe^{2+} + H_2O_2 + 2H^+ = 2Fe^{3+} + 2H_2O$. In the H_2O_2-free similar operations, the blank absorbance values for the possible oxidation of Fe^{2+} to Fe^{3+} by dissolved oxygen were recorded to be 0.0462 for standard H_2O_2-free solution (0 mM H_2O_2) and 0.0544 for the sample solution without PPEC-ORR, respectively, and such small absorbance should indicate that the effect of oxidation of Fe^{2+} to Fe^{3+} by dissolved oxygen is very small. Even so, our reference cell actually contained a mixture of 50 μL of ultrapure water and 450 μL of 1 M aqueous HCl containing 10 mM $FeSO_4$ (stayed for 30 min after mixing), thus any blank absorbance should have been corrected during recording the Fe^{3+} absorbance for determining H_2O_2.

Furthermore, CV experiments on an Au disk electrode were conducted to confirm the PPEC-ORR production of H_2O_2 in the photocathode compartment, since the unique CV peaks for the oxidation and reduction of H_2O_2 can be used to confirm the presence of H_2O_2, and the height of H_2O_2-oxidation peak can be used to quantify H_2O_2.

Table S1 A brief comparison of H_2O_2 synthesis by anthraquinone method and PEC method*

Method	**Main consumable items**	**Typical process for H_2O_2 synthesis**	**Wastewater discharge**
Anthraquinone method[4, 5]	2-Ethylanthraquinone, trioctyl phosphate, palladium, hydrogen, air, water and etc.	2-Ethylanthraquinone and trioctyl phosphate were prepared into a working solution. Under 0.3 MPa pressure, 55 ~ 65 ^{o}C temperature and palladium catalyst conditions, hydrogen gas was introduced into the solution for hydrogenation, followed by oxidation with air (or oxygen) at 40 ~ 44 ^{o}C, and then extraction, regeneration, refining and concentration to obtain a H_2O_2 aqueous solution.	Containing environmentally harmful organic compounds
PEC method[6, 7]	Sunlight, air, and water	Under the light irradiation condition, air (or oxygen) is introduced into an aqueous solution containing an appropriate supporting electrolyte, and a bias is applied using an electrochemical workstation to generate H_2O_2 on the photocathode and O_2 on the counter electrode	Almost no environmentally harmful products

*At present, the synthesis of H_2O_2 by anthraquinone method has the advantages of mature technology and high yield, but it has some deficiencies in energy consumption, cost (e.g., hydrogen source) and wastewater discharge. In contrast, the synthesis of H_2O_2 by PEC method has the advantages of green and sustainable energy, low cost and environmental friendliness, but the relatively low yield of H_2O_2 at present needs to be improved.

Table S2 Performance of H_2O_2 synthesis by either PEC-ORR or PPEC-ORR on representative photocathodes*

Method	**Photocathode**	**Electrolyte solution**	**Applied potential (V vs RHE)**	**Photocurrent density (mA cm^{-2})**	**H_2O_2 yield (mM cm^{-2} h^{-1})**	**Reference**
PEC-ORR	$CuBi_2O_{4,Gd}$/CuO/FTO	0.1 M KOH	0.4	-0.88	1.3	[3]
PEC-ORR	$CuFeO_2$/FTO	1 M NaOH	0.6	-0.712	1.04	[8]
PEC-ORR	$CuBi_2O_{4,F}$/FTO	0.1 M KOH	0.4	-0.574	0.85	[9]
PEC-ORR	Cu_3BiS_3/ITO	0.1 M PBS	0.4	-0.278	0.41	[7]
PEC-ORR	g-C_3N_4/$ZnWO_4$/ITO	0.1 M KOH	0.7	-0.305	0.45	[10]
PPEC-ORR	Au_{NP}/p-$ZnO_{Sb,NT}$/ITO	0.5 M Na_2SO_4	0.4	-1.05	1.52	This work

*For comparison with the previously reported H_2O_2 yields in mM cm^{-2} h^{-1}, the H_2O_2 yield of 15.2 μmol cm^{-2} h^{-1} in this research (10 mL solution volume) is converted to the H_2O_2 yield of 1.52 mM cm^{-2} h^{-1}. $CuBi_2O_{4,Gd}$: Gd-doped $CuBi_2O_4$, $CuBi_2O_{4,F}$: F-doped $CuBi_2O_4$. PBS: phosphate buffer solution. All the experiments here employed 100 mW cm^{-2} AM 1.5G simulated sunlight as the light source.

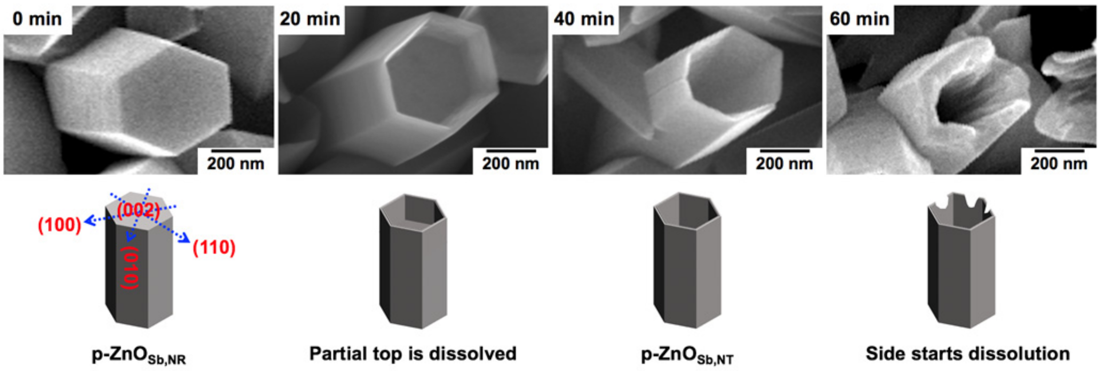

Fig. S1 SEM images (the top row) and schematic drawing (the bottom row) that show the etching of p-ZnO$_{Sb,NR}$ into p-ZnO$_{Sb,NT}$ in 0.15 M aqueous NaOH at 85 ^{o}C for typical etching time. There are two polar faces (top and bottom surfaces) and six nonpolar side faces in the hexagonal wurtzite ZnO, where the Zn-terminated polar face (002) is metastable and chemically active for the etching, while the nonpolar side faces (100, 010, 110) are more stable and more chemically inert for the etching.[11] Therefore, the etching rate of the metastable Zn-terminated polar face (002) is much faster than that of the nonpolar side faces (100, 010, 110), inducing the gradual dissolution of the ZnO nanorod core from the top towards the bottom.[12] When the etching time is less than 40 min, it is gradually etched along the top to the bottom of the ZnO nanorod core. When the etching time is equal to 40 min, the ZnO nanotubes with a hollow structure can be obtained, which is basically consistent with the results that the XRD peak corresponding to the (002) crystal plane of p-ZnO$_{Sb,NT}$/ITO is smaller than that of p-ZnO$_{Sb,NR}$/ITO, while the XRD peaks corresponding to the (100, 010, 110) crystal planes are basically unchanged (Fig. S2). When the etching time is greater than 40 min, the side of the top is also etched, and the integrity of the ZnO nanotubes begins to be destroyed.

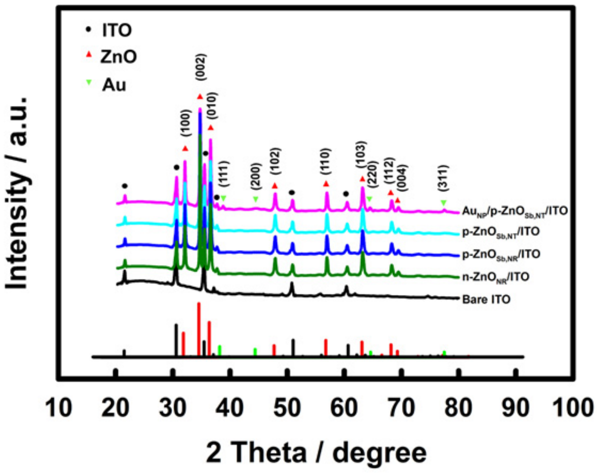

Fig. S2 XRD spectra of the bare ITO, n-ZnO$_{NR}$/ITO, p-ZnO$_{Sb,NR}$/ITO, p-ZnO$_{Sb,NT}$/ITO, and Au$_{NP}$/p-ZnO$_{Sb,NT}$/ITO electrodes. Here, the XRD peaks of bare ITO are in good agreement with those of standard ITO (JCPDS No. 71-2195). In addition to the XRD peaks of ITO, eight new XRD peaks at 31.8°, 34.4°, 36.3°, 47.5°, 56.6°, 62.9°, 68.0° and 69.2° on the n-ZnO$_{NR}$/ITO electrode can be assigned to the (100), (002), (010), (102), (110), (103), (112) and (004) crystal planes of ZnO, respectively, according to the standard card of hexagonal wurtzite structure ZnO (JCPDS No. 79-2205). These sharp XRD peaks indicate good crystallinity. There are no obvious XRD peaks of Sb on the p-ZnO$_{Sb,NR}$/ITO electrode, probably due to the amorphous structure of doped Sb.[13] On the p-ZnO$_{Sb,NT}$/ITO electrode, the weakening of the (002) diffraction peak is owing to the hollow nanotubes (NT) structure of p-ZnO$_{Sb,NT}$/ITO, as reported for the etching of n-ZnO$_{NR}$/ITO into n-ZnO$_{NT}$/ITO.[14] On the Au$_{NP}$/p-ZnO$_{Sb,NT}$/ITO electrode, in addition to the diffraction peaks of ITO and ZnO, four new peaks at 38.2°, 44.4°, 64.6° and 77.5° are assigned to the (111), (200), (220) and (311) crystal planes of Au, respectively, according to the standard card of Au (JCPDS No. 89-3697).

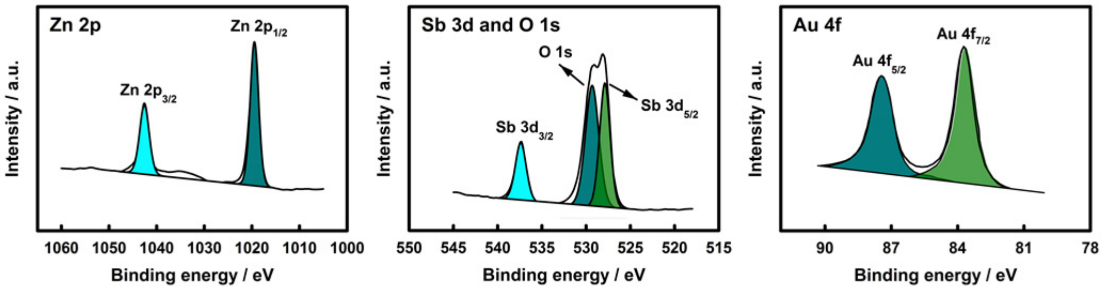

Fig. S3 XPS spectra of Zn 2p, Sb 3d and O 1s, and Au 4f of Au$_{NP}$/p-ZnO$_{Sb,NT}$/ITO electrode. Here, the two peaks at 1041.2 eV and 1021.5 eV are attributed to Zn 2P$_{1/2}$ and Zn 2P$_{3/2}$ of Zn^{2+}, respectively.[15] The peak at 538.1 eV is attributed to Sb 3d$_{3/2}$ of Sb^{3+}. The two peaks at 529.2 eV and 527.6 eV are attributed to O 1s of O^{2-} and Sb 3d$_{5/2}$ of Sb^{3+}, respectively, which is due to the partial overlap between Sb and O.[13] The two peaks at 87.7 eV and 83.3 eV are attributed to Au 4f$_{5/2}$ and Au 4f$_{7/2}$ of Au^0, respectively.[16]

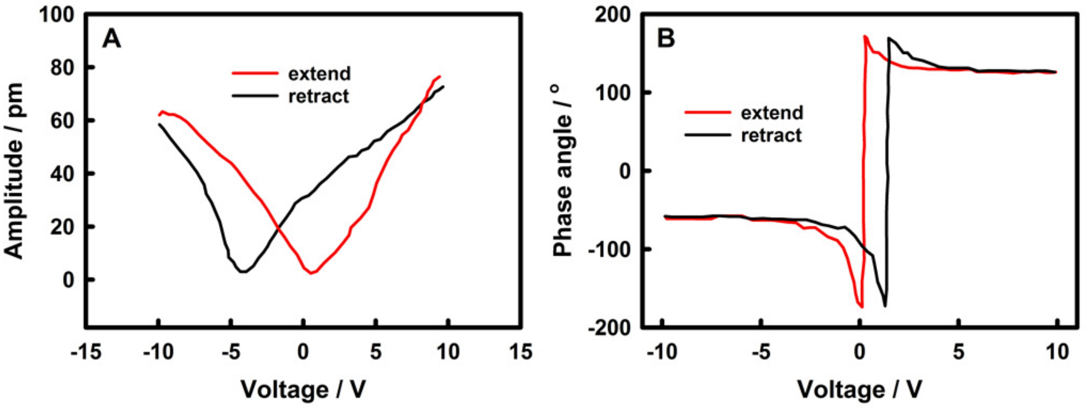

Fig. S4 PFM amplitude (A) and phase angle (B) versus voltage curves of the p-ZnO$_{Sb,NT}$/ITO electrode. Here, the amplitude curves of p-ZnO$_{Sb,NT}$/ITO electrode under alternating voltage excitation show a typical butterfly-shape, and the phase angle curves show a hysteresis loop, indicating that the p-ZnO$_{Sb,NT}$/ITO electrode has good piezoelectric activity.[17]

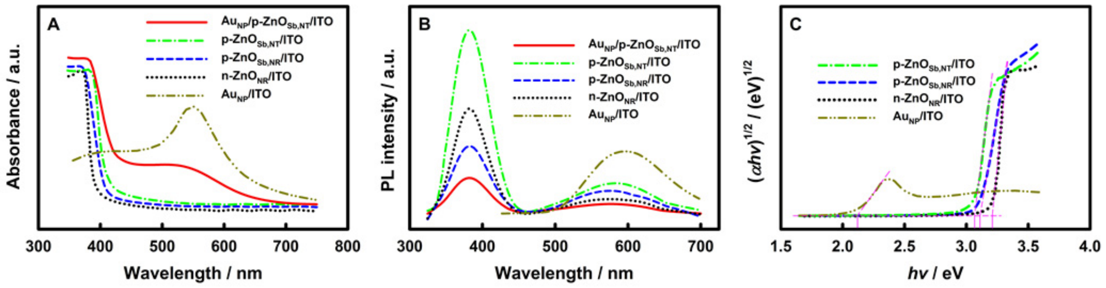

Fig. S5 (A) UV-vis DRS, (B) PL spectra and (C) Tauc curves of the n-ZnO_{NR}/ITO, p-$ZnO_{Sb,NR}$/ITO, p-$ZnO_{Sb,NT}$/ITO, Au_{NP}/p-$ZnO_{Sb,NT}$/ITO electrodes (excited at 325 nm) and Au_{NP}/ITO electrode (excited at 425 nm). Here, the n-ZnO_{NR}/ITO electrode shows two emission peaks at ca. 380 nm and ca. 580 nm,[18] due to the de-excitation of photoexcited electrons from the CB level (ca. 380 nm) and the defect level (ca. 580 nm) to the valence band (VB) level, respectively. The p-$ZnO_{Sb,NR}$/ITO electrode has a weakened emission peak at ca. 380 nm and a strengthened emission peak at ca. 580 nm, because a new defect level is generated in ZnO after Sb-doping, which reduces the quantity of photoexcited electrons on the CB level and increases the quantity of photoexcited electrons on the defect level. The emission peaks at ca. 380 nm and ca. 580 nm of the p-$ZnO_{Sb,NT}$/ITO electrode become stronger, because the band gap (E_g) of p-$ZnO_{Sb,NT}$ becomes smaller, and the number of photoexcited electrons on the CB level and the defect level is increased. The emission peaks of Au_{NP}/p-$ZnO_{Sb,NT}$/ITO electrode are both weaker at ca. 380 nm and ca. 580 nm, because the formation of Schottky barriers between Au_{NP} and p-$ZnO_{Sb,NT}$ can inhibit the recombination of photogenerated charges, and the localized surface plasmon resonance (LSPR) absorption peak of Au_{NP} and the visible light emission peak of p-$ZnO_{Sb,NT}$ can partially overlap.

The semiconductor's E_g can be calculated according to Eqs. S1 and S2,[1]

$$h\nu = hc/\lambda \text{ (J)} = hc/\lambda e \text{ (eV)} = 1240/\lambda \text{ (eV)} \tag{S1}$$

$$(\alpha hv)^{1/2} = k(hv - E_g) \qquad \text{(S2)}$$

where h is the Planck constant (6.626×10^{-34} J s), v is the frequency (Hz), λ is the wavelength (nm), e is the charge of a single electron (1.602×10^{-19} C), c is the light speed (2.998×10^{8} m s^{-1}), α is the absorption coefficient, k is a constant, and E_g is the band gap of semiconductor (eV).

According to Eqs. S1 and S2 and the UV-vis DRS curves, take hv as the abscissa and $(\alpha hv)^{1/2}$ as the ordinate to make Tauc curves, the intercept of the Tauc curve ramp's tangent line on the abscissa is the E_g of semiconductor. According to Eq. S2, when $(\alpha hv)^{1/2} = 0$, then $E_g = hv$, so the E_g values are 3.22 eV for n-ZnO$_{NR}$/ITO, 3.12 eV for p-ZnO$_{Sb,NR}$/ITO, 3.06 eV for p-ZnO$_{Sb,NT}$/ITO, and 2.13 eV for Au$_{NP}$/ITO, indicating that both the Sb-doping and the hollow NT structure can effectively reduce the E_g of ZnO, and Au$_{NP}$ can effectively improve the visible light absorption.

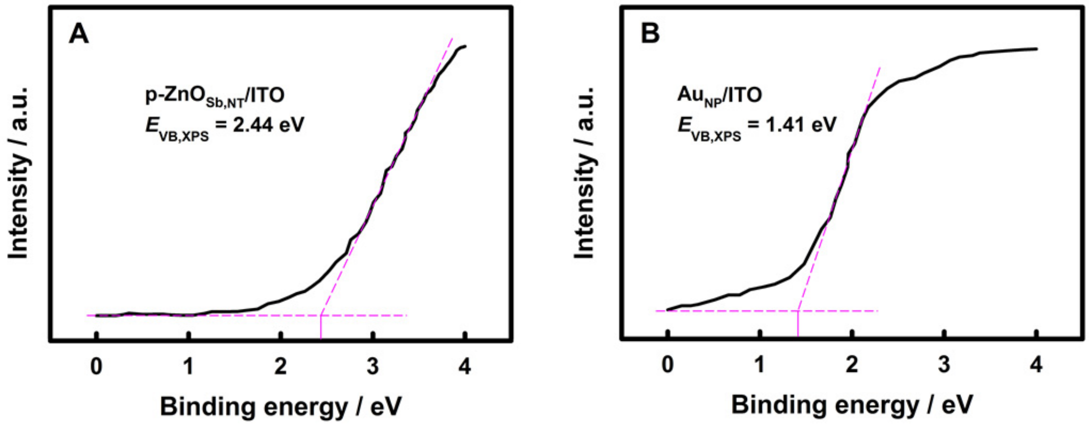

Fig. S6 VB XPS curves of p-ZnO$_{Sb,NT}$/ITO (A) and Au$_{NP}$/ITO (B) electrodes. Here, the valence band ($E_{VB,RHE}$) of a semiconductor can be calculated according to Eq. S3,[19]

$$E_{VB,RHE} = E_{VB,XPS} + \varphi - 4.44 \tag{S3}$$

where $E_{VB,RHE}$ is the E_{VB} vs RHE, $E_{VB,XPS}$ is the binding energy at the intersection point between the tangent line of the ramp and the abscissa in the VB XPS curves (here $E_{VB,XPS}$ = 2.44 eV for p-ZnO$_{Sb,NT}$/ITO and $E_{VB,XPS}$ = 1.41 eV for Au$_{NP}$/ITO), and φ is the instrument work function (4.6 eV).

According to Eq. S3, we obtain $E_{VB,RHE}$ = 2.60 eV for p-ZnO$_{Sb,NT}$/ITO and $E_{VB,RHE}$ = 1.57 eV for Au$_{NP}$/ITO. According to $E_g = E_{VB} - E_{CB}$ and the E_g values obtained from Fig. S5, the E_{CB} values are -0.46 eV for p-ZnO$_{Sb,NT}$/ITO and -0.56 eV for Au$_{NP}$/ITO.

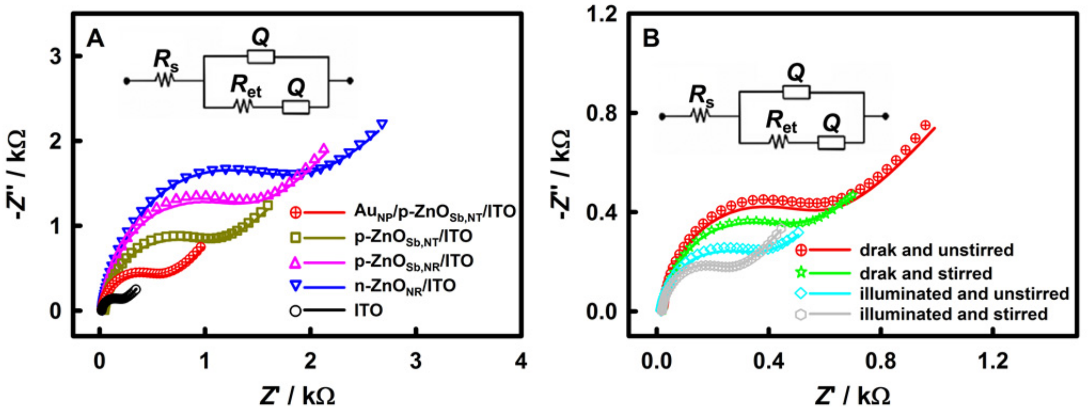

Fig. S7 (A) EIS curves of the bare ITO, n-ZnO_{NR}/ITO, p-$ZnO_{Sb,NR}$/ITO, p-$ZnO_{Sb,NT}$/ITO and Au_{NP}/p-$ZnO_{Sb,NT}$/ITO electrodes in 0.5 M aqueous Na_2SO_4 containing 2.0 mM $K_4[Fe(CN)_6]$ under dark and unstirred conditions; (B) EIS curves of Au_{NP}/p-$ZnO_{Sb,NT}$/ITO electrode in 0.5 M aqueous Na_2SO_4 containing 2.0 mM $K_4[Fe(CN)_6]$ either without stirring or stirred at 1500 rpm (dark and unstirred; dark and stirred; illuminated and unstirred; or illuminated and stirred). Illumination: 100 mW cm^{-2} AM 1.5G simulated sunlight. Initial potential = 0.24 V vs Ag/AgCl(sat.) (formal potential), quiet time = 200 s (to ensure a 1:1 $[Fe(CN)_6]^{3-/4-}$ concentration ratio near the electrode surface during EIS measurements), and amplitude =10 mV. Symbols: experimental; curves: fitted to the modified Randles equivalent circuit (Inset). Here, the R_{et} values follow the order n-ZnO_{NR}/ITO (2.36 kΩ) > p-$ZnO_{Sb,NR}$/ITO (1.98 kΩ) > p-$ZnO_{Sb,NT}$/ITO (1.24 kΩ) > Au_{NP}/p-$ZnO_{Sb,NT}$/ITO (0.813 kΩ) > ITO (0.144 kΩ), because the R_{et} value can be increased after decreasing the electron-conductance of electrode surface by modifying the semiconductor n-ZnO_{NR} on ITO, but the electron-conductance of electrode surfaces may be increased and the R_{et} values can be decreased after loading Sb-doped p-$ZnO_{Sb,NR}$, p-$ZnO_{Sb,NT}$ obtained after chemical etching to form a hollow structure, and/or photodeposited Au_{NP}. The R_{et} values follow the order Au_{NP}/p-$ZnO_{Sb,NT}$/ITO (dark and unstirred, 0.813 kΩ) > Au_{NP}/p-$ZnO_{Sb,NT}$/ITO (dark and stirred, 0.631 kΩ) > Au_{NP}/p-

$ZnO_{Sb,NT}$/ITO (illuminated and unstirred, 0.468 kΩ) > Au_{NP}/p-$ZnO_{Sb,NT}$/ITO (illuminated and stirred, 0.382 kΩ), because solution stirring can bend the piezoelectrically active p-$ZnO_{Sb,NT}$ to generate piezoelectric charges, and light illumination can lead to the separation and transfer of photogenerated charges of p-$ZnO_{Sb,NT}$.

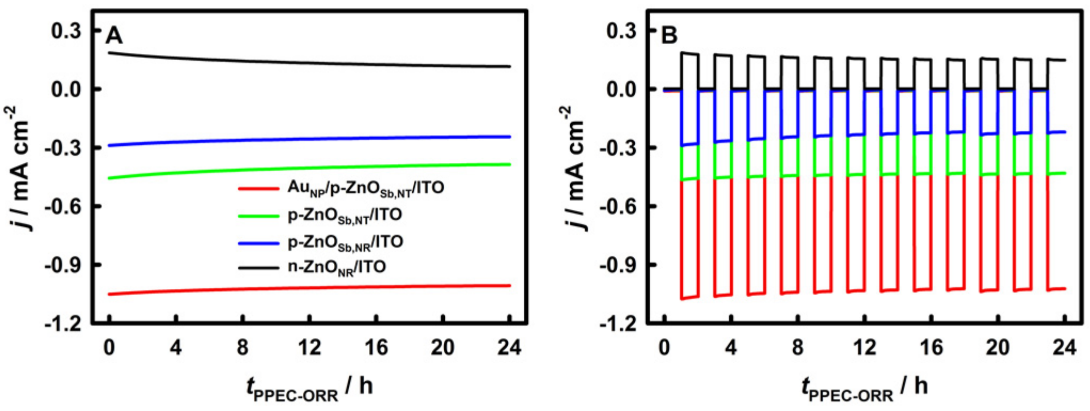

Fig. S8 *j*-*t* curves under continuous light illumination (A) and under chopped-light illumination (B, 1 h switch time) of the n-ZnO$_{NR}$/ITO, p-ZnO$_{Sb,NR}$/ITO, p-ZnO$_{Sb,NT}$/ITO and Au$_{NP}$/p-ZnO$_{Sb,NT}$/ITO electrodes at 0.4 V vs RHE in O_2-saturated 0.5 M aqueous Na_2SO_4 stirred at 1500 rpm, under 100 mW cm^{-2} AM 1.5G simulated sunlight illumination.

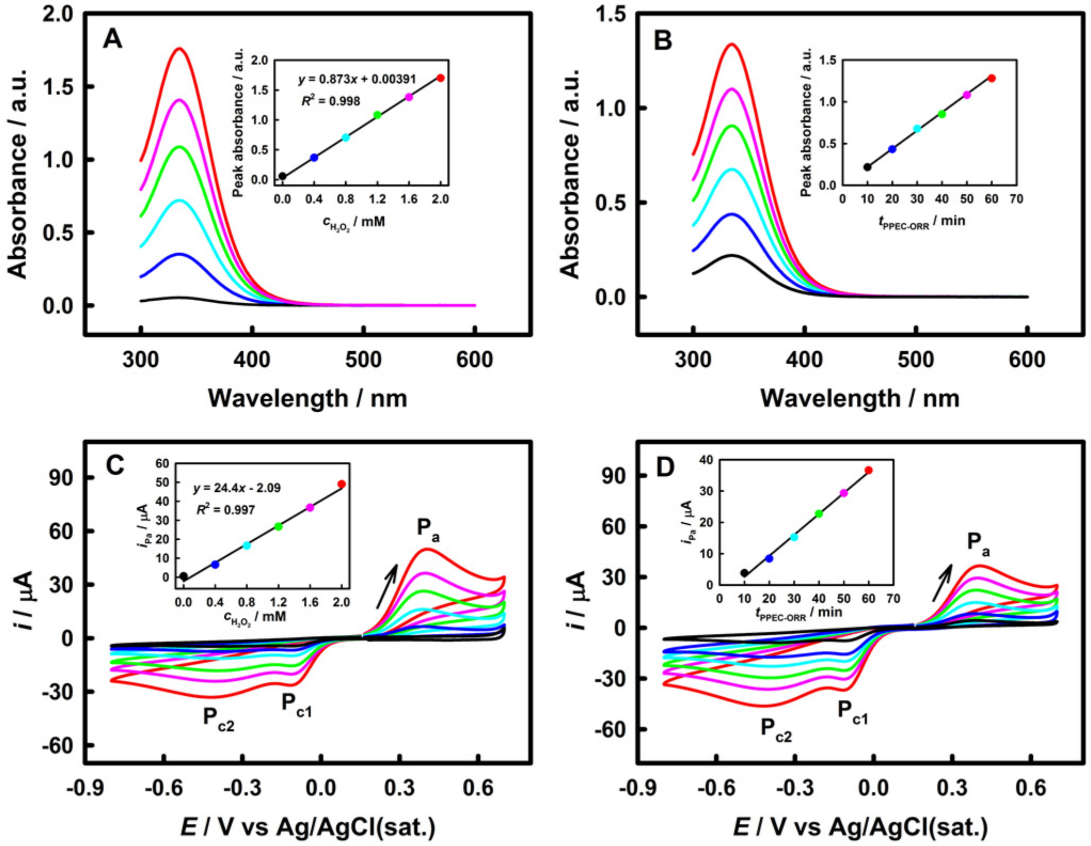

Fig. S9 UV-vis absorption spectra of Fe^{3+} generated by the $FeSO_4$-H_2O_2 redox reaction for standard (A, a series of prepared standard H_2O_2 solutions) or sample (B, the photocathode solution after different PPEC-ORR time) H_2O_2 solutions. The insets show the linear relationship of the peak absorbance at 330 nm versus H_2O_2 concentration (c_{H2O2}) or PPEC-ORR time ($t_{PPEC-ORR}$). CV curves at a bare Au disk electrode (3 mm diameter) in 0.5 M aqueous Na_2SO_4 containing standard (C, air-saturated, prepared by adding H_2O_2) or sample (D, oxygen-saturated photocathode solution after different PPEC-ORR time) H_2O_2. Scan rate: 50 mV s^{-1}. The insets show the linear relationship of the anodic H_2O_2-oxidation peak (P_a) current (i_{pa}, background not corrected) at ca. 0.41 V vs Ag/AgCl/KCl(sat.) versus H_2O_2 concentration or PPEC-ORR time. Here, the air-saturated (panel C) or oxygen-saturated (panel D) 0.5 M Na_2SO_4 blank aqueous solution gave negligible currents near P_a, a very small cathodic O_2-reduction peak (P_{c1}, reduction of dissolved O_2 into H_2O_2), and a very small cathodic H_2O_2-reduction peak (P_{c2}, and the H_2O_2 comes from the reduction of dissolved O_2 into H_2O_2). In vivid contrast, 0.5 M aqueous Na_2SO_4 containing standard H_2O_2 (panel C) or sample H_2O_2 (panel D) showed the obvious anodic H_2O_2-oxidation peak (P_a, and i_{pa} is proportional to the standard H_2O_2 concentration or the PPEC-ORR time), a notable cathodic O_2-reduction peak (P_{c1}, reduction of the original dissolved O_2 plus the O_2 generated under P_a into H_2O_2), and a notable cathodic H_2O_2-reduction peak (P_{c2}, where the H_2O_2 comes from both the H_2O_2 generated during the reduction of O_2 under P_{c1} and the original H_2O_2, and here the original H_2O_2 comes from either PPEC-ORR or standard addition). The CV curves of the H_2O_2-containing solutions (panels C and D) are in good agreement with those reported previously,[20] solidly confirming the PPEC-ORR production of H_2O_2 in the photocathode compartment. In addition, we have proven that, from the standard curves shown in panels A and C, UV-vis spectrophotometry and CV (i_{pa}) can quantitatively return almost identical H_2O_2 concentrations in the photocathode compartment solution, and thus the concentrations of H_2O_2 determined by UV-vis spectrophotometry are reported in this research.

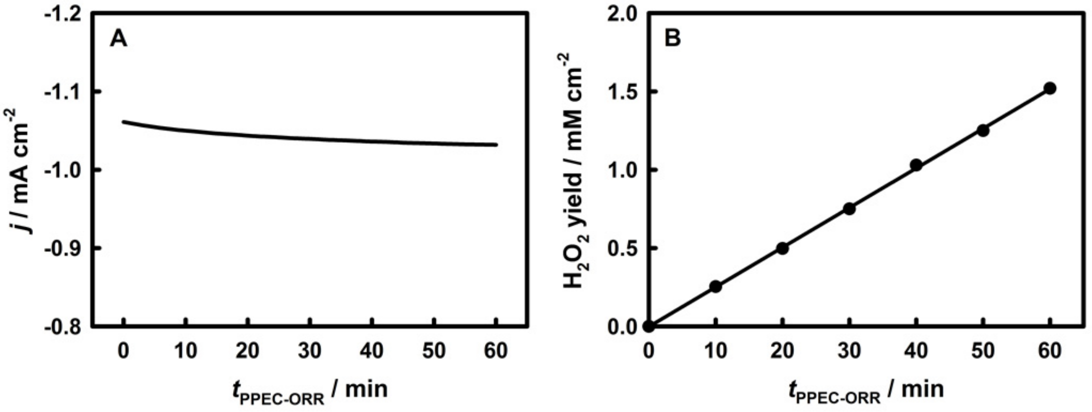

Fig. S10 Photocurrent density (A) and H_2O_2 yield (B) on the Au_{NP}/p-$ZnO_{Sb,NT}$/ITO electrode at 0.4 V vs RHE in O_2-saturated 0.5 M aqueous Na_2SO_4 stirred at 1500 rpm under 100 mW cm^{-2} AM 1.5G simulated sunlight illumination. Here, the molar concentration of H_2O_2 generated by PPEC and ORR is determined by UV-vis spectrophotometry of Fe^{3+} based on the $FeSO_4$-H_2O_2 redox reaction, as detailed in Fig. S9. The molar concentration of Fe^{3+} produced after the $FeSO_4$-H_2O_2 redox reaction (c_{Fe3+}) can be calculated according to the Lambert-Beer law (Eq. S4),

$$A = Kbc_{Fe3+} \tag{S4}$$

where A is the peak absorbance of Fe^{3+} at 330 nm, K is the molar absorption coefficient of Fe^{3+}, b is the thickness of the Fe^{3+} solution layer that absorbs light, and c_{Fe3+} is the concentration of light absorbing substance Fe^{3+}.

The corresponding molar quantity of H_2O_2 (n) can be obtained by UV-vis spectrophotometry of Fe^{3+} based on the $FeSO_4$-H_2O_2 redox reaction $2Fe^{2+} + H_2O_2 + 2H^+ = 2Fe^{3+} + 2H_2O$. The electric charge ($Q'$) corresponding to the ORR generation of n mol H_2O_2 can be obtained from the Faraday law of electrolysis, $Q' = zFn$, where z is the number of electrons transferred during ORR ($z = 2$) and F is the Faraday constant (96485.3 C mol^{-1}). The Faraday efficiency (η) is thus calculated according to Eq. S5,

$$\eta = Q'/Q \times 100\% \quad \text{(S5)}$$

where Q is the experimental electric charge by integrating the photocurrent versus time curve, as shown in Fig. S10A. Since PEC involves the complicated energy conversion among light energy, electrical energy and chemical energy, the η here is, in our opinion, only an apparent Faraday efficiency.

At 60 min in Fig. S10B, we obtain n = 15.2 μmol, Q' = 2.93 C, and Q = 3.71 C, so η = 79.0%. Here, the η value of 79.0% is reasonable, as many reports on different materials and systems have the PEC (or PPEC) η values located between ca. 65% and ca. 90%.[7, 21-24]

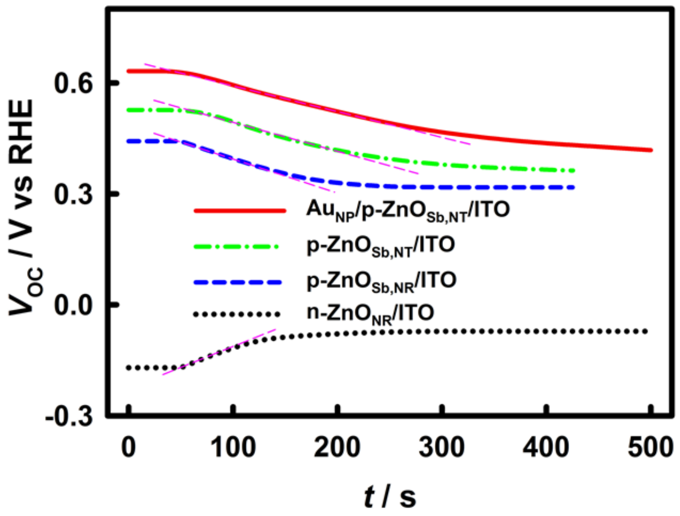

Fig. S11 V_{OC}-t curves of the n-ZnO_{NR}/ITO, p-$ZnO_{Sb,NR}$/ITO, p-$ZnO_{Sb,NT}$/ITO and Au_{NP}/p-$ZnO_{Sb,NT}$/ITO electrodes in O_2-saturated 0.5 M aqueous Na_2SO_4 stirred at 1500 rpm after 100 mW cm^{-2} AM 1.5G simulated sunlight illumination for 50 s. Here, the photoelectron lifetime (τ, in s) of a semiconductor can be calculated from Eq. S6,[25]

$$\tau = (k_B T/e) \times |dV_{OC}/dt|^{-1} \tag{S6}$$

where k_B is the Boltzmann constant (1.381×10^{-23} J K^{-1}), T is the temperature (298 K), e is the charge of a single electron (1.602×10^{-19} C), t is the time (s), and V_{OC} is the open circuit potential (V). The absolute value sign here implies that τ is always a positive value regardless of the positive or negative value of dV_{OC}/dt.

The dV_{OC}/dt values of 1.14×10^{-3} V s^{-1} for n-ZnO_{NR}/ITO, -8.97×10^{-4} V s^{-1} for p-$ZnO_{Sb,NR}$/ITO, -8.23×10^{-4} V s^{-1} for p-$ZnO_{Sb,NT}$/ITO, and -7.38×10^{-4} V s^{-1} for Au_{NP}/p-$ZnO_{Sb,NT}$/ITO are obtained from the slopes of the ramps. The τ values of 23 ns for n-ZnO_{NR}/ITO, 29 ns for p-$ZnO_{Sb,NR}$/ITO, 31 ns for p-$ZnO_{Sb,NT}$/ITO, and 35 ns for Au_{NP}/p-$ZnO_{Sb,NT}$/ITO are thus obtained, implying the best PPEC performance on the Au_{NP}/p-$ZnO_{Sb,NT}$/ITO electrode at 1500 rpm (due to the largest τ).

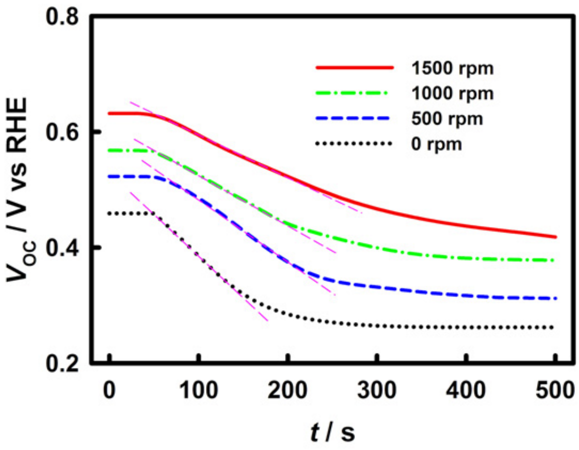

Fig. S12 V_{OC}–t curves of the Au_{NP}/p-$ZnO_{Sb,NT}$/ITO electrode in O_2-saturated 0.5 M aqueous Na_2SO_4 stirred at 0, 500, 1000, or 1500 rpm after 100 mW cm^{-2} AM 1.5G simulated sunlight illumination for 50 s. After the calculations similar to those in Fig. S11, the τ values of the Au_{NP}/p-$ZnO_{Sb,NT}$/ITO electrode at different solution-stirring rates are obtained as 35 ns at 1500 rpm, 29 ns at 1000 rpm, 24 ns at 500 rpm, and 17 ns at 0 rpm, implying the best PPEC performance on the Au_{NP}/p-$ZnO_{Sb,NT}$/ITO electrode at 1500 rpm (due to the largest τ).

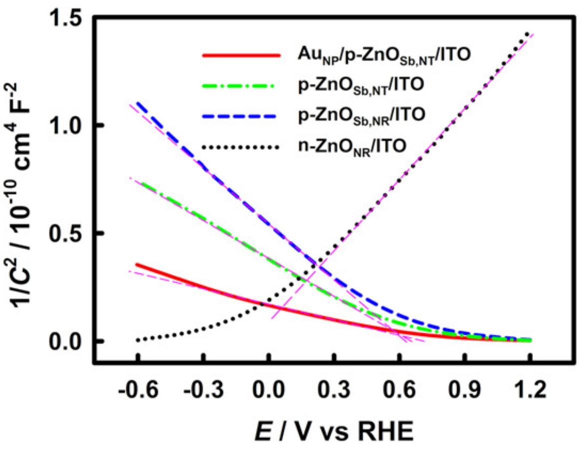

Fig. S13 Mott-Schottky curves of the n-ZnO_{NR}/ITO, p-$ZnO_{Sb,NR}$/ITO, p-$ZnO_{Sb,NT}$/ITO and Au_{NP}/p-$ZnO_{Sb,NT}$/ITO electrodes in O_2-saturated 0.5 M aqueous Na_2SO_4 stirred at 1500 rpm.

Here, the carrier density (N, in cm^{-3}) of a semiconductor can be calculated from Eq. S7,[26]

$$N = [2/(e\varepsilon\varepsilon_0)] \times |\mathrm{d}(1/C^2)/\mathrm{d}E|^{-1} \qquad \text{(S7)}$$

where e is the charge of a single electron (1.602×10^{-19} C), ε is the relative permittivity (10 for ZnO[27]), ε_0 is the permittivity of vacuum (8.854×10^{-14} F cm^{-1}), E is the potential (V), and C is the capacitance density (F cm^{-2}). The absolute value sign here implies that N is always a positive value regardless of the positive or negative value of $\mathrm{d}(1/C^2)/\mathrm{d}E$.

From the slopes of the ramps and Eq. S7, we obtain the $\mathrm{d}(1/C^2)/\mathrm{d}E$ (in cm^4 F^{-2} V^{-1}) and N (in cm^{-3}) values of 1.13×10^{10} cm^4 F^{-2} V^{-1} and 1.25×10^{21} cm^{-3} for n-ZnO_{NR}/ITO, -8.23×10^9 cm^4 F^{-2} V^{-1} and 1.71×10^{21} cm^{-3} for p-$ZnO_{Sb,NR}$/ITO, -6.10×10^9 cm^4 F^{-2} V^{-1} and 2.31×10^{21} cm^{-3} for p-$ZnO_{Sb,NT}$/ITO, as well as -2.41×10^9 cm^4 F^{-2} V^{-1} and 5.85×10^{21} cm^{-3} for Au_{NP}/p-$ZnO_{Sb,NT}$/ITO electrodes. The larger N value indicates that more photogenerated carriers are available for PEC applications, thus the above results imply the best PPEC performance on the Au_{NP}/p-$ZnO_{Sb,NT}$/ITO electrode at 1500 rpm.

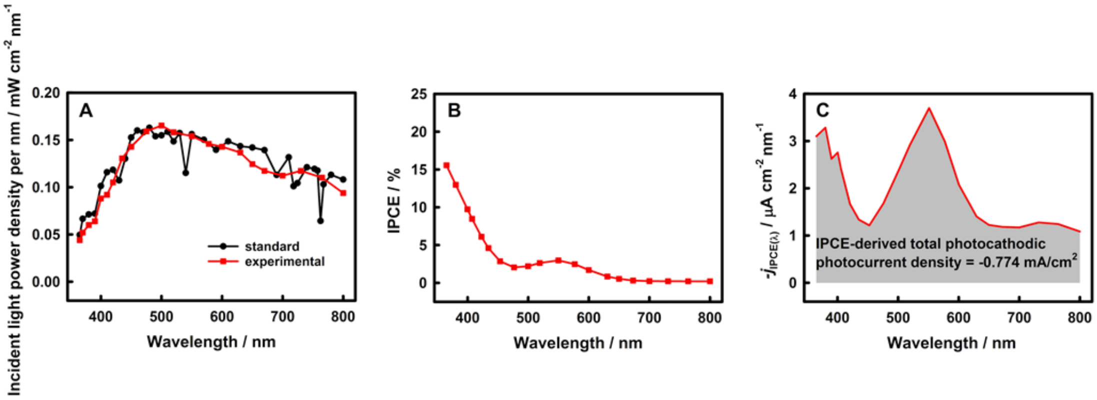

Fig. S14 (A) Incident light power density per nm versus incident light wavelength measured by using a series of optical filters (5 nm bandwidth, from 365 to 800 nm) and an optical power density meter under 100 mW cm^{-2} AM 1.5G simulated sunlight illumination, and the standard 100 mW cm^{-2} AM 1.5G simulated solar spectrum in this wavelength range is shown for comparison. (B) IPCE curve of the Au_{NP}/p-$ZnO_{Sb,NT}$/ITO electrode, which is a copy of Fig. 3B (Au_{NP}/p-$ZnO_{Sb,NT}$/ITO), but the wavelength data points corresponding to Fig. S14A are labeled in Fig. S14B for the calculation of Fig. S14C. (C) IPCE-derived photocurrent density per nm ($j_{IPCE}(\lambda)$, calculated from the data shown in Fig. S14A and Fig. S14B according to Eqs. S8-S13 below) versus incident light wavelength for the Au_{NP}/p-$ZnO_{Sb,NT}$/ITO electrode.

Here, we measured the spectrum of incident light power density per nm versus incident light wavelength by using a series of optical filters (5 nm bandwidth, from 365 to 800 nm) and an optical power density meter under 100 mW cm^{-2} AM 1.5G simulated sunlight, which agrees well with the standard 100 mW cm^{-2} AM 1.5G simulated solar spectrum in this wavelength range,[28] as shown in Fig. S14A. As shown in Figs. S14B and 3B (Au_{NP}/p-$ZnO_{Sb,NT}$/ITO), the IPCE values of the Au_{NP}/p-$ZnO_{Sb,NT}$/ITO electrode at different wavelength were measured on the ZAHNER electrochemical workstation. The IPCE-derived photocurrent density per nm ($j_{IPCE}(\lambda)$) versus incident light wavelength (Fig. S14C) can be calculated as follows from the incident light power densities (Fig. S14A) and the IPCE values (Fig. S14B) at different wavelength.

The IPCE-derived photocurrent density ($j_{\mathrm{IPCE}}(\lambda)$) of a semiconductor can be calculated according to Eqs. S8-S13,[29]

$$\mathrm{IPCE}(\lambda) = \frac{N_\mathrm{e}}{N_\mathrm{p}} \times 100\% \qquad \text{(S8)}$$

$$N_\mathrm{e} = \frac{j_{\mathrm{IPCE}}(\lambda) \times t}{e} \qquad \text{(S9)}$$

$$N_\mathrm{p} = \frac{P(\lambda) \times t}{h \times v} \qquad \text{(S10)}$$

$$v = \frac{c}{\lambda} \qquad \text{(S11)}$$

$$\mathrm{IPCE}(\lambda) = \frac{\frac{j_{\mathrm{IPCE}}(\lambda) \times t}{e}}{\frac{P(\lambda) \times t \times \lambda(\text{in m})}{h \times c}} = \frac{j_{\mathrm{IPCE}}(\lambda) \times h \times c}{P(\lambda) \times e \times \lambda(\text{in m})} = \frac{j_{\mathrm{IPCE}}(\lambda)}{P(\lambda) \times \lambda(\text{in m})} \times \frac{h \times c}{e}$$

$$= \frac{j_{\mathrm{IPCE}}(\lambda)}{P(\lambda) \times \lambda(\text{in m})} \times \frac{6.626 \times 10^{-34} \times 2.998 \times 10^{8}}{1.602 \times 10^{-19}} = \frac{j_{\mathrm{IPCE}}(\lambda)}{P(\lambda) \times \lambda(\text{in m})} \times 12.4 \times 10^{-7}$$

$$= \frac{j_{\mathrm{IPCE}}(\lambda) \times 1240}{P(\lambda) \times \lambda(\text{in nm})} \times 100\% \qquad \text{(S12)}$$

$$j_{\mathrm{IPCE}}(\lambda) = \pm\frac{\mathrm{IPCE}(\lambda) \times \lambda \times P(\lambda)}{1240} \text{ (positive for photoanode and negative for photocathode)} \qquad \text{(S13)}$$

where IPCE(λ) is the incident photon-electron conversion efficiency at incident light wavelength (%), λ is the incident light wavelength (nm), N_e is the number of electrons, N_p is the number of photons, $j_{\mathrm{IPCE}}(\lambda)$ is the IPCE-derived photocurrent density per nm at incident light wavelength (mA cm^{-2} nm^{-1}, note here that it is logically defined as a positive value for photoanode and a negative value for photocathode), t is the time (s), e is the charge of a single electron (1.602 × 10^{-19} C), $P(\lambda)$ is the incident light power density at incident light wavelength (mW cm^{-2}), h is the Planck constant (6.626 × 10^{-34} J s), v is the incident light frequency (Hz), and c is the light speed (2.998 × 10^{8} m s^{-1}).

As shown in Fig. S14C, the IPCE-derived total photocathodic photocurrent density, calculated by integrating $j_{\mathrm{IPCE}}(\lambda)$ from 365 nm to 800 nm, is -0.774 mA cm^{-2}, which is, as expected, somewhat smaller than but still comparable with the experimental PPEC photocathodic photocurrent density of -1.05 mA cm^{-2}, because the PPEC measurement was carried out under AM 1.5G simulated sunlight (ideally with full wavelength from ca. 305 nm to ca. 4045 nm, actually from 300 nm to 1100 nm for our light source), while the wavelength range of IPCE light source is only from 365 nm to 800 nm. The IPCE-derived total photocathodic photocurrent density of -0.774 mA cm^{-2} and the experimental PPEC photocathodic photocurrent density of -1.05 mA cm^{-2} are thus rational, indicating the reliability of the PPEC data on the Au$_{NP}$/p-ZnO$_{Sb,NT}$/ITO electrode.

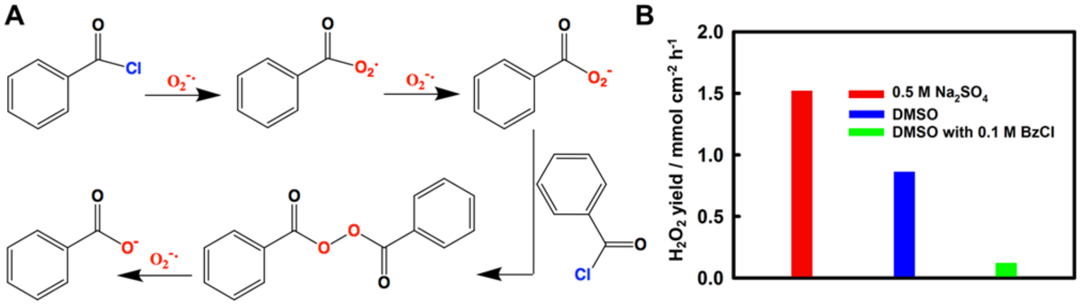

Fig. S15 (A) Reaction scheme of benzoyl chloride with superoxide radical anion in DMSO containing 0.1 M Bu_4NPF_6.[7] (B) H_2O_2 yield in 1 h PPEC-ORR on Au_{NP}/p-$ZnO_{Sb,NT}$/ITO electrode at 0.4 V vs RHE in O_2-saturated 0.5 M aqueous Na_2SO_4, DMSO, or DMSO containing 0.1 M BzCl. All solutions were stirred at 1500 rpm under 100 mW cm^{-2} AM 1.5G simulated sunlight illumination. Here, the H_2O_2 yield in nonaqueous dimethyl sulfoxide (DMSO) containing 0.1 M tetrabutylammonium hexafluorophosphate (Bu_4NPF_6) was smaller than that in 0.5 M aqueous Na_2SO_4, due probably to some degree of hydrophilicity of the Au_{NP}/p-$ZnO_{Sb,NT}$/ITO electrode surface. The H_2O_2 yield was further reduced after 0.1 M benzoyl chloride (BzCl) was added, due to the capture of superoxide radical anion ($O_2^{\cdot-}$) by BzCl to inhibit the further reduction of $O_2^{\cdot-}$ to H_2O_2, proving that $O_2^{\cdot-}$ is an important intermediate in the PPEC-ORR process.

References (The numbering here is only valid for the Electronic Supplementary Information)

1. X. Zhang, Y. Liu and Z. H. Kang, *ACS Appl. Mater. Interfaces*, 2014, **6**, 4480-4489.
2. B. Liu and E. S. Aydil, *J. Am. Chem. Soc.*, 2009, **131**, 3985-3990.
3. Z. X. Li, Q. L. Xu, F. L. Gou, B. He, W. Chen, W. W. Zheng, X. Jiang, K. Chen, C. Z. Qi and D. K. Ma, *Nano Research*, 2021, **14**, 3439-3445.
4. G. H. Gao, Y. N. Tian, X. X. Gong, Z. Y. Pan, K. Y. Yang and B. N. Zong, *Chinese Journal of Catalysis*, 2020, **41**, 1039-1047.
5. H. B. Li, B. Zheng, Z. Y. Pan, B. N. Zong and M. H. Qiao, *Frontiers of Chemical Science and Engineering*, 2018, **12**, 124-131.
6. Y. Xue, Y. T. Wang, Z. H. Pan and K. Sayama, *Angew. Chem. Int. Edit.*, 2021, **60**, 10469-10480.
7. C. Chen, M. Yasugi, L. Yu, Z. Y. Teng and T. Ohno, *Applied Catalysis B-Environmental*, 2022, **307**, 121152.
8. A. Yengantiwar, P. S. Shinde, S. L. Pan and A. Gupta, *J. Electrochem. Soc.*, 2018, **165**, H831-H837.
9. Y. L. Xu, Z. X. Li, X. Hu, X. Wu, W. Chen, S. J. Zhou, J. J. Li, C. Z. Qi and D. K. Ma, *J. Catal.*, 2022, **410**, 339-346.
10. Z. Y. Zhu, F. Zhou, S. Zhan, N. B. Huang and Q. C. He, *Appl. Surf. Sci.*, 2018, **456**, 156-163.
11. X. Y. Gan, X. M. Li, X. D. Gao and W. D. Yu, *J. Alloys Compd.*, 2009, **481**, 397-401.
12. H. D. Yu, Z. P. Zhang, M. Y. Han, X. T. Hao and F. R. Zhu, *J. Am. Chem. Soc.*, 2005, **127**, 2378-2379.

13. C. Cao, X. X. Xie, Y. M. Zeng, S. H. Shi, G. Z. Wang, L. Yang, C. Z. Wang and S. W. Lin, *Nano Energy*, 2019, **61**, 550-558.
14. W. C. Lee, Y. X. Fang, R. Kler, G. E. Canciani, T. C. Draper, Z. T. Y. Al-Abdullah, S. M. Alfadul, C. C. Perry, H. Y. He and Q. Chen, *Mater. Chem. Phys.*, 2015, **149**, 12-16.
15. Z. Q. Liu, L. X. Ding, Z. L. Wang, Y. C. Mao, S. L. Xie, Y. M. Zhang, G. R. Li and Y. X. Tong, *Crystengcomm*, 2012, **14**, 2289-2295.
16. T. Wang, B. J. Jin, Z. B. Jiao, G. X. Lu, J. H. Ye and Y. P. Bi, *Chem. Commun.*, 2015, **51**, 2103-2106.
17. J. X. Xiao, T. S. Herng, J. Ding and K. Y. Zeng, *Acta Mater.*, 2017, **123**, 394-403.
18. Z. J. Bao, X. Y. Xu, G. Zhou and J. G. Hu, *Nanotechnology*, 2016, **27**, 305403.
19. Y. L. Xing, G. Ni, J. Liu, Y. P. Tian and W. X. Que, *Appl. Surf. Sci.*, 2018, **458**, 464-477.
20. T. T. Zhang, Y. Xing, Y. Song, Y. Gu, X. Y. Yan, N. N. Lu, H. Liu, Z. Q. Xu, H. X. Xu, Z. Q. Zhang and M. Yang, *Anal. Chem.*, 2019, **91**, 10589-10595.
21. T. H. Jeon, B. Kim, C. Kim, C. Xia, H. T. Wang, P. J. J. Alvarez and W. Choi, *Energ. Environ. Sci.*, 2021, **14**, 3110-3119.
22. T. Ouyang, Y. Q. Ye, C. H. Tan, S. T. Guo, S. Huang, R. Zhao, S. L. Zhao and Z. Q. Liu, *J. Phys. Chem. Lett.*, 2022, **13**, 6867-6874.
23. K. Zhang, J. L. Liu, L. Y. Wang, B. J. Jin, X. F. Yang, S. L. Zhang and J. H. Park, *J. Am. Chem. Soc.*, 2020, **142**, 8641-8648.

24. D. Li, D. Chandra, K. Saito, T. Yui and M. Yagi, *Nanoscale Research Letters*, 2014, **9**, 542.

25. J. Bisquert, A. Zaban, M. Greenshtein and I. Mora-Sero, *J. Am. Chem. Soc.*, 2004, **126**, 13550-13559.

26. F. X. Xiao and B. Liu, *Nanoscale*, 2017, **9**, 17118-17132.

27. S. C. Zhang, Z. F. Liu, M. N. Ruan, Z. G. Guo, L. E, W. Zhao, D. Zhao, X. F. Wu and D. M. Chen, *Applied Catalysis B-Environmental*, 2020, **262**.

28. J. W. Sun, D. K. Zhong and D. R. Gamelin, *Energ. Environ. Sci.*, 2010, **3**, 1252-1261.

29. X. Wang, C. Liow, D. Qi, B. Zhu, W. R. Leow, H. Wang, C. Xue, X. Chen and S. Li, *Adv. Mater.*, 2014, **26**, 3506-3512.